12-19-2016

Skull Shape Affects Susceptibility to Traumatic Brain Injury

Kashyap Arcot
Washington University in St. Louis

Guy M. Genin
Washington University in St. Louis

Skull shape affects susceptibility to traumatic brain injury

Kashyap Arcot and Guy M. Genin

Abstract

Rapid deformation of brain matter caused by skull acceleration is one of the most significant causes of concussion and severe traumatic brain injury (TBI). Despite substantial research being conducted in this area of study, very little is understood regarding the mechanics of the brain when exposed to rapid acceleration. As a result, the biomechanics of TBI remain ambiguous. In the present study, we apply a new strain estimation algorithm that enables the tracking of strains on the periphery of an image onto data obtained from tagged gel phantom and human MR-images. We use this new method to quantify strain concentrations at the brain-skull interface, and observe the interactions between the brain and the connective tissue that anchors it inside the skull. Our results allow us to noninvasively observe and quantify the biomechanical response of the brain to rapid skull movement. We find that the sub-arachnoid space creates regions of high strain magnitudes due to its anatomical makeup, and that the *falx cerebri* creates regions of high strain due to its inhibition of brain motion. Additionally, we see that skull shape significantly affects the transmission of strains at the brain-skull interface, and that certain skull shapes create localized concentrations of high strains. Our results imply that skull shape plays an important role in affecting sensitivity to acceleration among individuals, and may increase the likelihood of TBI in the event of an accident.

1. Introduction

In the United States alone, an estimated 1.7 million cases of traumatic brain injury (TBI) arise every year. Within these cases, over 50,000 patients die, 270,000 patients are hospitalized, and over 1.3 million are treated at an emergency department[1]. In 2010, the estimated economic cost of TBI was over $76 billion, with 90% of these costs attributed to fatal or hospitalized cases[2,3]. Due to its significant impact on human

health, substantial research has been conducted in regards to the causes and effects of TBI, however the results have been largely inconclusive. This is due in part to the brain's complex structure and composition, making it a very difficult organ to study in motion. Over the past decade, research has shifted to a mechanical approach to studying TBI, with an emphasis on strain fields in the brain as a metric of brain injury. Studies have shown that the likelihood of brain injury can be predicted by local strains and strain rates, measured during rapid skull acceleration[4,5,9]. As a result, the use of strains in measuring brain damage has become widely adopted in various fields of research[6,7,8].

A significant challenge to studying TBI is the inaccessibility of the brain. The mechanics of brain motion and deformation are due in large part to the anchoring of the brain to the skull. This connection is governed by various layers of connective tissue that make up the dura, arachnoid, and pia mater, as well as cerebrospinal fluid (CSF) that flows freely through the sub-arachnoid space (the area between the arachnoid mater and pia mater). The structural integrity of the connective tissue and the presence of CSF greatly affects the mechanics of the brain-skull interface, which is ultimately what governs brain motion and deformation in response to rapid accelerations. In animal and cadaver studies, the mechanical properties of the dura, arachnoid, and pia mater are drastically altered, and the absence of CSF dries out the brain, severely compromising the accuracy of any strain fields obtained from brain motion. Due to the importance of maintaining the brain's compositional integrity, studies have largely shifted to noninvasive methods of analyzing brain deformation, namely through the use of Magnetic Resonance (MR) images.

By combining tagged MR-images of viscoelastic gel phantoms with Fourier-based strain measurement techniques, quantitative strain fields describing basic brain-like movement were first developed[10,11]. This same method was then extended to MR-images of a human brain, and revealed patterns of strain fields that were comparable to the gel phantom studies[12,13]. The most significant limitation posed by this method is the inability to generate accurate strain fields at the periphery of the images. Fourier-based techniques for calculating strain are extremely reliable for rectangular shaped objects, but begin to lose their accuracy very quickly as the boundary conditions increase in complexity. Even for simple polygons composed of multiple rectangles, Fourier-based techniques were shown to have difficulty generating accurate strain fields at the boundaries[14]. *In* vivo, the brain's structural integrity relies largely on its anchoring to the skull, which occurs only at the boundaries (i.e., the brain-skull interface). This boundary is dependent on the behavior of connective tissue, CSF flowing through the sub-arachnoid space, and the general shape of the skull, which varies from patient to patient. These factors result in extremely complex mathematical boundary conditions that Fourier-based strain measurement techniques are unable to understand. As a result, the most crucial aspect of brain behavior during TBI has remained unclear.

Here, we overcome this significant obstacle to understanding brain deformation via a novel method of generating strain fields. Through the use of a Direct Deformation Estimation (DDE) algorithm that circumvents the need to calculate displacement fields before estimating strain fields, paired with a Strain Interference with Measures of Probable Local Elevation (SIMPLE) algorithm that distinguishes high concentrations of strain due to errors, we are able to generate accurate strain patterns in irregularly shaped objects all the way to their periphery, and study the behavior of the brain-skull interface during rapid acceleration of the skull. We present the application of this new set of algorithms onto tagged MR-images of both gel phantoms and human brains. Through the use of DDE and SIMPLE, we are able to see a clear elevation of strains in the sub-arachnoid space of human brains, as well as localized strain concentrations that arise through interactions between the brain and its boundary.

2. Methods

2.1 Obtaining tagged MR-images from a gel viscoelastic cylinder

The procedure to obtain the phantom MR-images is identical to one conducted in a previous study[11]; these methods are summarized here.

Gelatin was poured in a capped acrylic cylinder (11.43 cm inner diameter, 12.7 cm outer diameter, 18 cm long) following the manufacturer's protocol (57.6 g of gelatin powder per liter of distilled water, heated to 80°C) and allowed to set at 10°C for a period of 18 hours prior to a test. The cylinder was attached to a custom MR-compatible rotation constraint device (Fig. 1-a), and placed on the bed of the MR scanner and moved into the scanner bore. The rotation device then induced a mild controlled angular acceleration in the gelatin (Fig. 1-c). A uniaxial accelerometer (PCB Model 336C04, PCB Piezotronics, Depew NY, range 5000 m/s^2) was mounted to the rotating holder and aligned with the direction of motion at a radius of 10.4 cm from the axis of rotation. The accelerometer was secured with a thin layer of petro wax (PCB Piezotronics, Depew NY). Data was collected at 10,000 samples/sec with a laptop PC-based data acquisition system (DAQCard 6062E, National Instruments, Austin, TX). Over a series of 30 trial impacts, the average peak deceleration recorded from the device was 27.7 m/s^2, with a standard deviation of 3.5 m/s^2. Mean (± std. deviation) angular acceleration, calculated from the average peak deceleration divided by the 10.4 cm offset of the accelerometer from the axis of rotation, was 266 ± 35 radians/s^2.

Tag lines (additional variations in brightness that are noninvasively superimposed onto MR-images) were used as markers for tracking motion of the cylinder. To produce these tag lines, a pair of radiofrequency (RF) pulses was applied in combination with magnetic gradients. This combination of RF pulses and magnetic gradients imposes temporary sinusoidal variations in the longitudinal magnetization of hydrogen nuclei (protons), which are the source of the signal in MR imaging. These variations lead to differences in intensity which move with the tissue. Tag line spacing was 10 mm between intensity peaks. A fast gradient-echo MR imaging sequence (FLASH 2D) was used to collect tagged images of the gel cylinder in a 1.5T MR Scanner (Sonata, Siemens, Malvern, PA).

2.2 Obtaining tagged MR-images from human subjects

The procedure to obtain tagged MR-images is identical to one conducted in a previous study[12]; these methods are summarized here.

Three adult male subjects of average height and weight (age 25-42 yrs; 70-80 kg; 1.7 – 1.8 m tall), performed controlled head rotation using a custom, MR-compatible device (Fig 1-a) that imparted a repeatable mild angular acceleration of ~250-300 rad/s^2. The protocol was reviewed and approved by the Washington University Human Research Protection Office. The head cylinder, which cradles the subject's head, was designed to fit inside the head coil of a Siemens Sonata MRI (Siemens, Munich, Germany) and rotate freely about a plastic bearing at the back of the device. Rotation was initiated by releasing a latch, which allowed the plastic counterweight to apply torque to the head cylinder Release of the latch also tripped a fiber optic switch that activated a TTL pulse to the MRI, initiating the scanning sequence. After approximately 200 ms, the weight impacted a stop pin, imparting an impulse to the rotating assembly. The associated angular deceleration produced measurable deformation in the subject's brain. The magnitudes of angular acceleration experienced by each subject were found by recording the linear tangent acceleration at a site on the head cylinder 10 cm from the axis of rotation. The duration of the peak acceleration pulse was approximately 40 ms. The magnitude of angular acceleration for subject S1 was 299 ± 29 rad/s^2; for subject S2, it was 244 ± 7 rad/s^2; and for subject S3, 370 ± 21 rad/s^2 (mean ± std. deviation).

The FLASH2D MR cine sequence was used to collect tagged images of the deformed brain. The sequence had a frame rate of 6 ms and an echo time TE= 2.9 ms. For each nominally identical repetition of the head rotation, a single line of k-space data (192 samples) was collected 90 times; each acquisition separated by 6 ms. The phase encoding-gradient was incremented after each repetition of motion. In total,

144 rotations of the head were required, leading to a 192×144 data matrix (image) for each of the 90 time points. To superimpose tag lines on the image, immediately after the latch was released, radio-frequency (RF) pulses were applied in combination with magnetic gradients. This sequence causes longitudinal magnetization of spins to vary spatially in a sinusoidal fashion[18], resulting in an image superimposed with an array of light and dark lines. These "tag lines" move with the tissue, and their intersections may be tracked to characterize motion. Images were collected in an axial plane 2 cm above the corpus callosum.

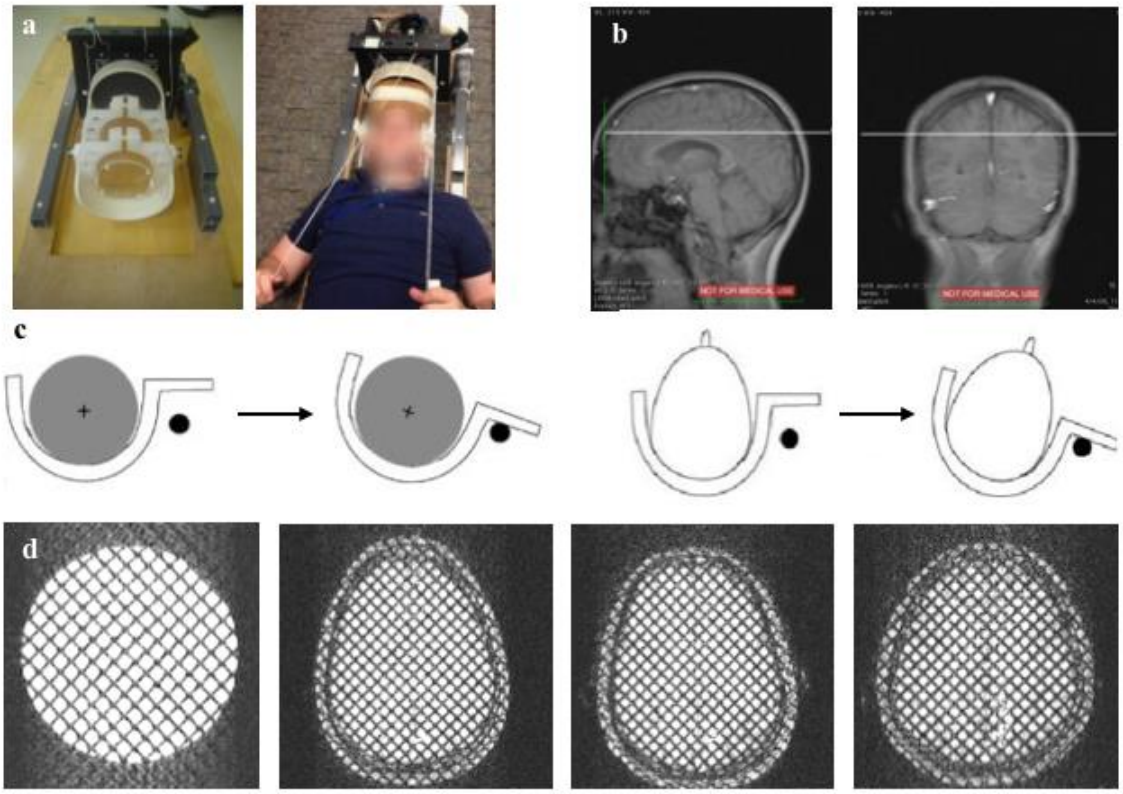

Figure 1 | Experimental protocol. (a) Custom MR-compatible head rotation constraint devices fabricated to enable repeated rotations of a gel phantom (left) and human head (right). **(b)** localizing MR-scans of one subject showing the location of the imaging plane, approximately 2 cm above the corpus callosum. **(c)** Schematics demonstrating the direction of gel phantom (left) and head (right) rotation **(d)** Tagged MR-images of gel phantom (left) and three human subjects (from left to right: subject 1, subject 2, subject 3) at rest, prior to rotation.

2.3 Masking surrounding noise from tagged MR-images

Four sets of DICOM data (obtained from MR-imaging the gel phantom and three human subjects) were losslessly converted to TIFF images. Each TIFF image was then opened in MATLAB, and a polygon was constructed around the boundary of the object being studied. The polygon was used to create a new image consisting of ones inside the area of the polygon, and zeros everywhere else. The two images were then combined, resulting in a new image consisting only of the tagged MR-image being studied, with all other data removed. This new image was then written as a TIFF image file. This function was applied to all four data sets (Supp Fig. 1).

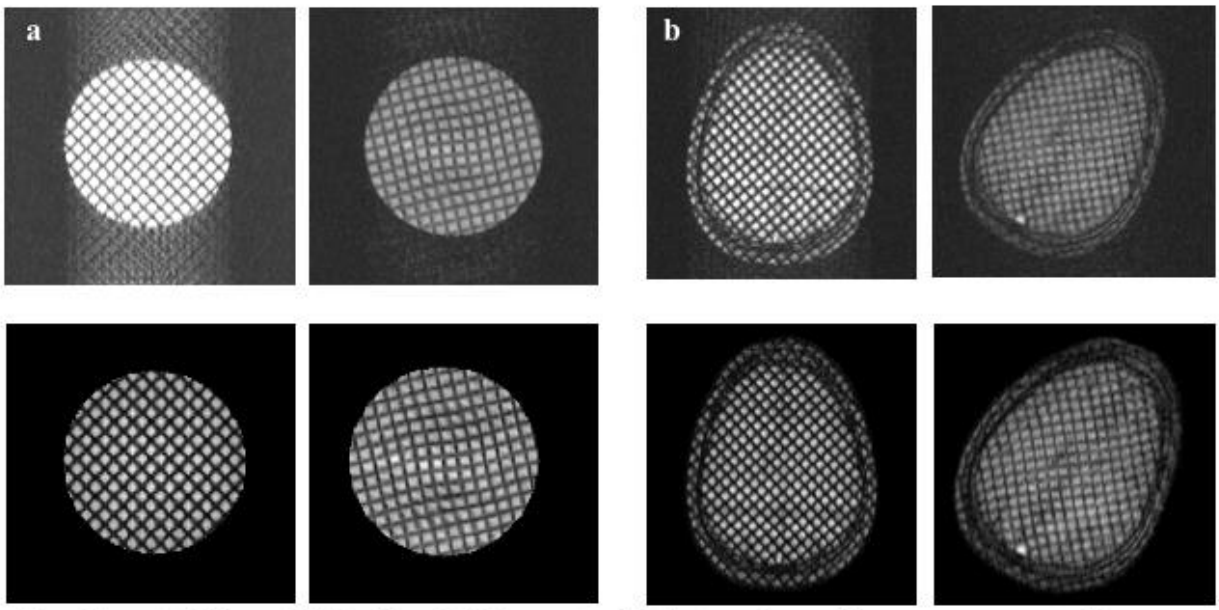

Supplemental Figure 1 | Masking MR-images to eliminate noise and improve accuracy of tracking. (a) Un-masked MR-images of gel phantom (top) and corresponding MR-Images after application of a masking function (bottom). From left to right: at rest, at peak positive rotation. **(b)** Un-maksed MR-images of human brain (top) and corresponding MR-Images after application of a masking function (bottom). From left to right: at rest, at peak positive rotation.

2.4 Using DDE and SIMPLE to obtainin strain fields of gel viscoelastic cylinder

The gel phantom data was run through a MATLAB program that analyzes movement of a specified region (either in a video or a collection of images) and creates a video of the strain field surrounding said region as it deforms[17]. The code relies on an optimized form of the Lucas-Kanade (LK) method for tracking optic flow, which altogether skips the estimation of displacement fields before generating strain fields and greatly increases the accuracy of the tracking method. The first image in the series was opened in MATLAB, and a polygon was created around the region of interest. For the gel phantom, the region of interest was the entire tagged image extending to to the boundary. A set of tag lines were then overlayed onto the image, which tracked movement of pixels as the program looped through each image in the data set (Supp Fig. 2-a). 2D strain tensors were calculated for every point within the region of interest in each frame, and corresponding strain fields were generated using heat maps. The output then generated a video that displays each frame in the data set with a strain field overlaid onto the image. Data was generated for strains in Cartesian coordinates (ε_{xx}, ε_{yy}, and ε_{xy}), and principal strains (ε_I ε_{II}).

2.5 Using DDE and SIMPLE to obtain strain fields of human subjects

The MR-images obtained from human subjects were run through the same MATLAB program, but required a few additional steps due to their complexity. The region of interest was first set to be the entire tagged image, extending to the periphery of the skull. DDE tag lines were overlaid onto the first image in the data set (Supp Fig 2-b), and attempted to track deformation of the image as the program looped through each image in the data set. The code was optimized until the program was tracking deformation without presenting any errors. This procedure was then repeated for a region consisting of only the brain parenchyma, and then repeated a final time for a region consisting of only the brain-skull interface (sub-arachnoid space). Data was generated for strains in Cartesian coordinates (ε_{xx}, ε_{yy}, and ε_{xy}), and principal strains (ε_I ε_{II}).

An analysis of strains at the brain-skull interface was conducted by calculating the average first principal strain magnitudes across the brain parenchyma, and comparing this to the magnitude of first principal strain along the sub-arachnoid space. A *p*-value test was conducted to determine if the differences in strain magnitudes was significant. A 99% confidence interval was used to conduct the test.

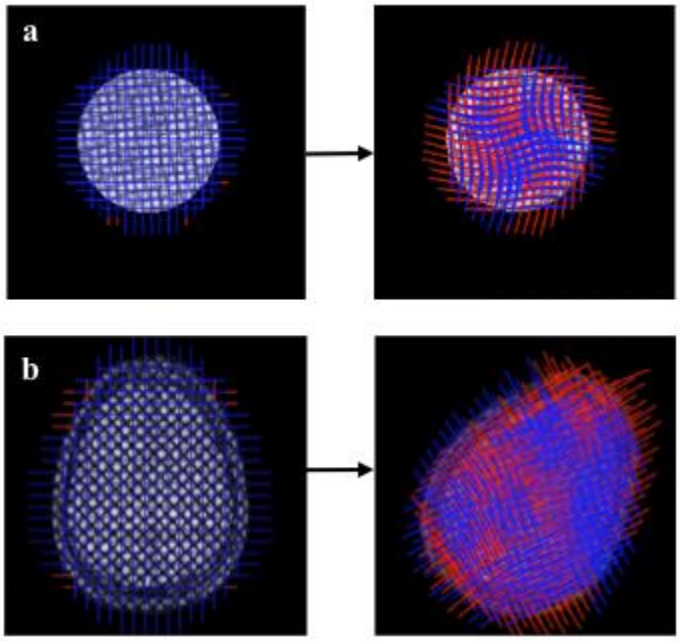

Supplemental Figure 2 | DDE algorithm used to track deformation of tagged MR-Images . (a) DDE lines overlaid onto an MR-Image of a gel phantom at rest (left), and at peak negative rotation (right). **(b)** DDE lines overlaid onto an MR-Image of a human brain at rest (left) and at peak positive rotation (right).

2.6 Optimization of DDE and SIMPLE on brain MR-images

In order to ensure that we were obtaining the most detailed strain fields without error, we created an optimization technique to find the ideal settings to run the program for each data set. We varied the number of pixels analyzed by each sub-region in the DDE algorithm and calculated the associated strain energy via the following formula:

$$\frac{\sum_{i=1}^{\#regions}(\epsilon_I(i)^2+\epsilon_{II}(i)^2)}{Area} \qquad \text{(I)}$$

We found that when too few pixels were analyzed in each sub-region, a very large strain energy was present, associated with large errors in strain calculations. With very small sub-regions, we observed increasingly noisy strain fields with very little reliable data (Supp Fig 3-a). We found that this was due to substantial mis-tracking as a result of broken tag lines (Supp Fig 3-b). We also found that when too few pixels were analyzed in each sub-region, a lack of data resulted in very low strain energies, and strain fields that provided no useful information. Using these results, we were able to quantify the accuracy of our results based on the size of our sub-regions, and identify an optimized range for collecting data (Supp Fig. 3-c).

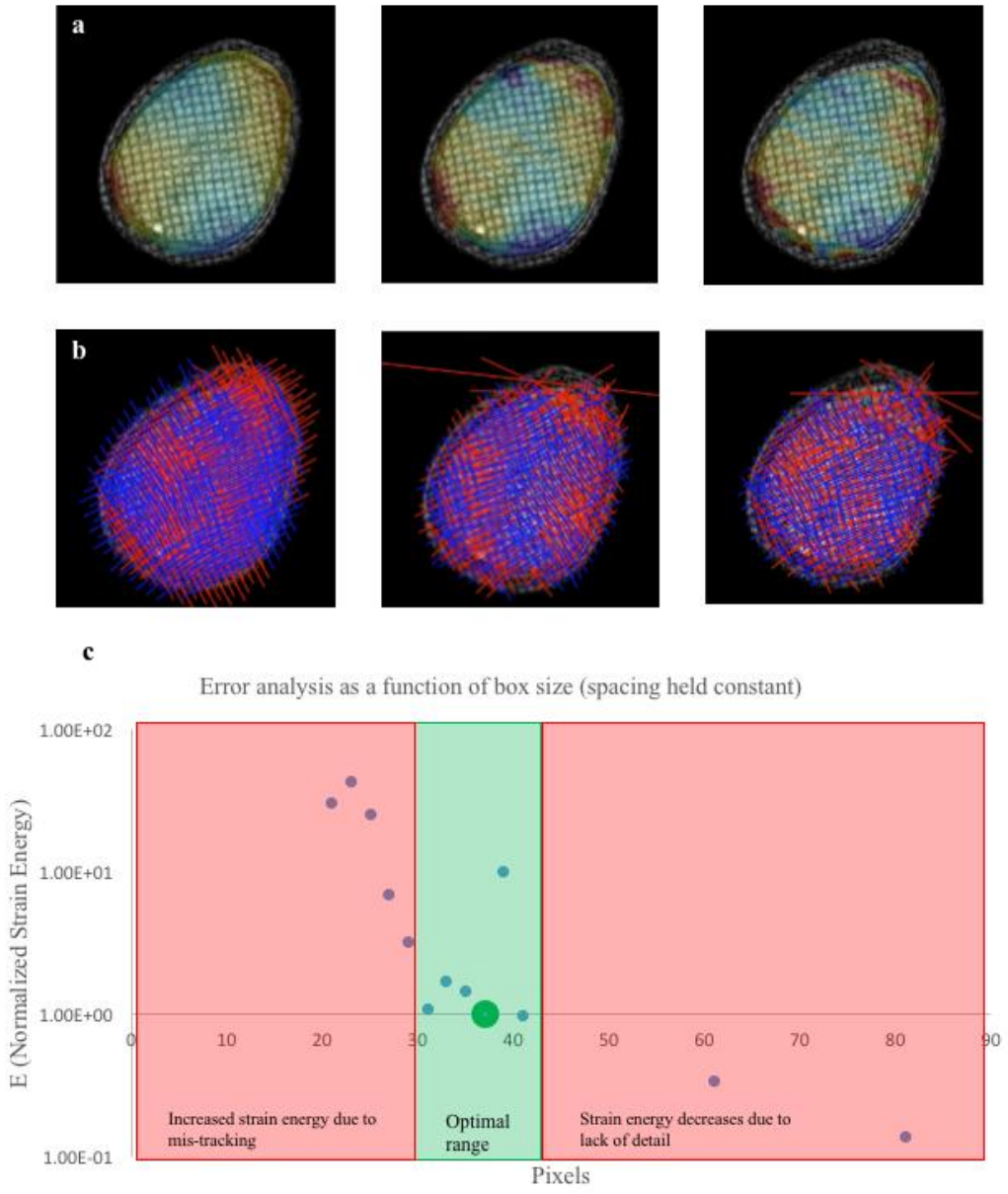

Supplemental Figure 3 | Error analysis of DDE and SIMPLE algorithms on human brain subject. (a) Lagrangian strain (ε_{xx}) of human subject 1 at peak positive rotation. **(b)** DDE lines attempting to track deformation at peak positive rotation. Box size from left to right: 37, 25, 21. Spacing held constant at 6.833. **(c)** Strain energy of human subject 1 as a function of boz size. Spacing held constant at 6.83. Ratio of Box Size to spacing was held constant at 6:1, and values were increased until the DDE algorithm was first able to successfully track deformation of the brain (occurred when box size was set to 41 and spacing was set to 6.833). Following this, the spacing was kept constant (6.833) while the box size was increased until the DDE algorithm was able to successfully track deformation for three consecutive trials of increasing box size without error (represented by the green data point).

3. Results

3.1 DDE and SIMPLE algorithms are able to obtain accurate strain patterns at the periphery of a gel viscoelastic cylinder

We applied the DDE and SIMPLE algorithms to a set of tagged MR-images used in a previous study of brain deformation, whereby a gel viscoelastic cylinder was subjected to rapid angular acceleration. In the previous study, strain fields were simulated using a nonlinear Finite Element (FE) model of a three-parameter "standard" linear viscoelastic cylinder[11]. At peak negative rotation, Lagrangian strain fields generated by DDE were identical to the simulated results, revealing a symmetric pattern of elevated strains near the boundary, with minimal strains closer to the center of the cylinder (Fig. 2). We observed strain magnitudes ranging from -0.1 to 0.1, which occurred in organized clusters near the periphery of the cylinder.

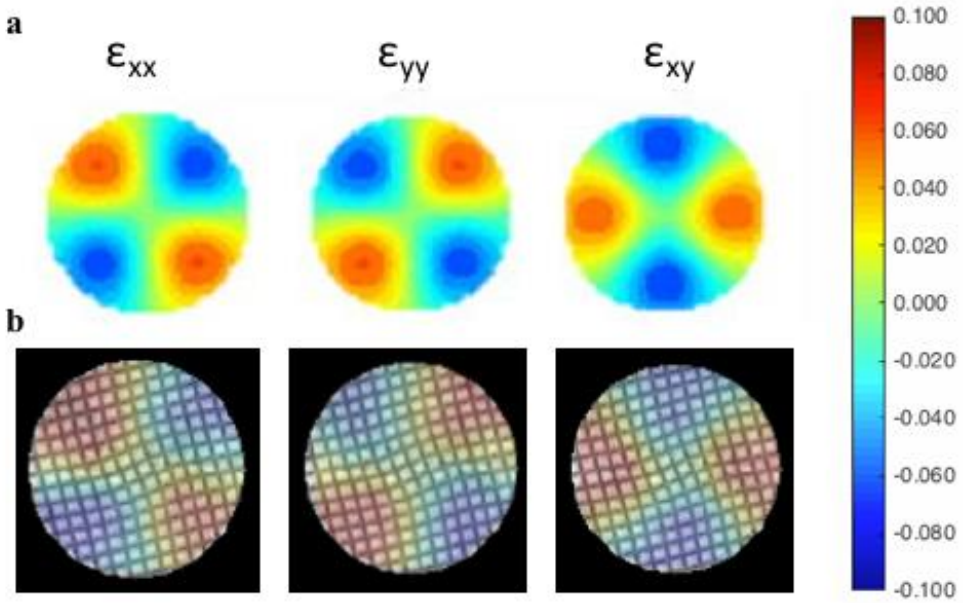

Figure 2 | SIMPLE and DDE estimates of a viscoelastic gel phantom at peak negative rotation. **(a)** Components of the Lagrangian strain tensor from nonlinear simulation. **(b)** Corresponding components of Lagrangian strain tensor using DDE and SIMPLE algorithms, with accurate strain fields extending to the boundary of the image.

3.2 Angular acceleration of the brain reveals consistent strain patterns across subjects

When applied to tagged MR-images of three separate human brains, DDE and SIMPLE revealed consistent and symmetric Lagrangian strain patterns in a Cartesian coordinate system across three different subjects (Fig. 3), comparable to the results obtained from the gel phantom study (Fig. 2). At peak positive rotation, we observed minimal strains at the center of the brain, with high strain magnitudes concentrated at the brain-skull interface. In subjects 1 and 2, we observed elevated shear strain (ε_{xy}) near the distal end of the *falx cerebri*, where the left and right hemispheres of the brain are separated. In subject 3, we observed a substantial rise in normal strain in the x-direction (ε_{xx}) at the proximal end of the right hemisphere relative to the other two subjects, which was accompanied by an expected rise in shear strain (ε_{xy}). This concentration of high strains resulted in a lack of elevated strains near the *falx cerebri*.

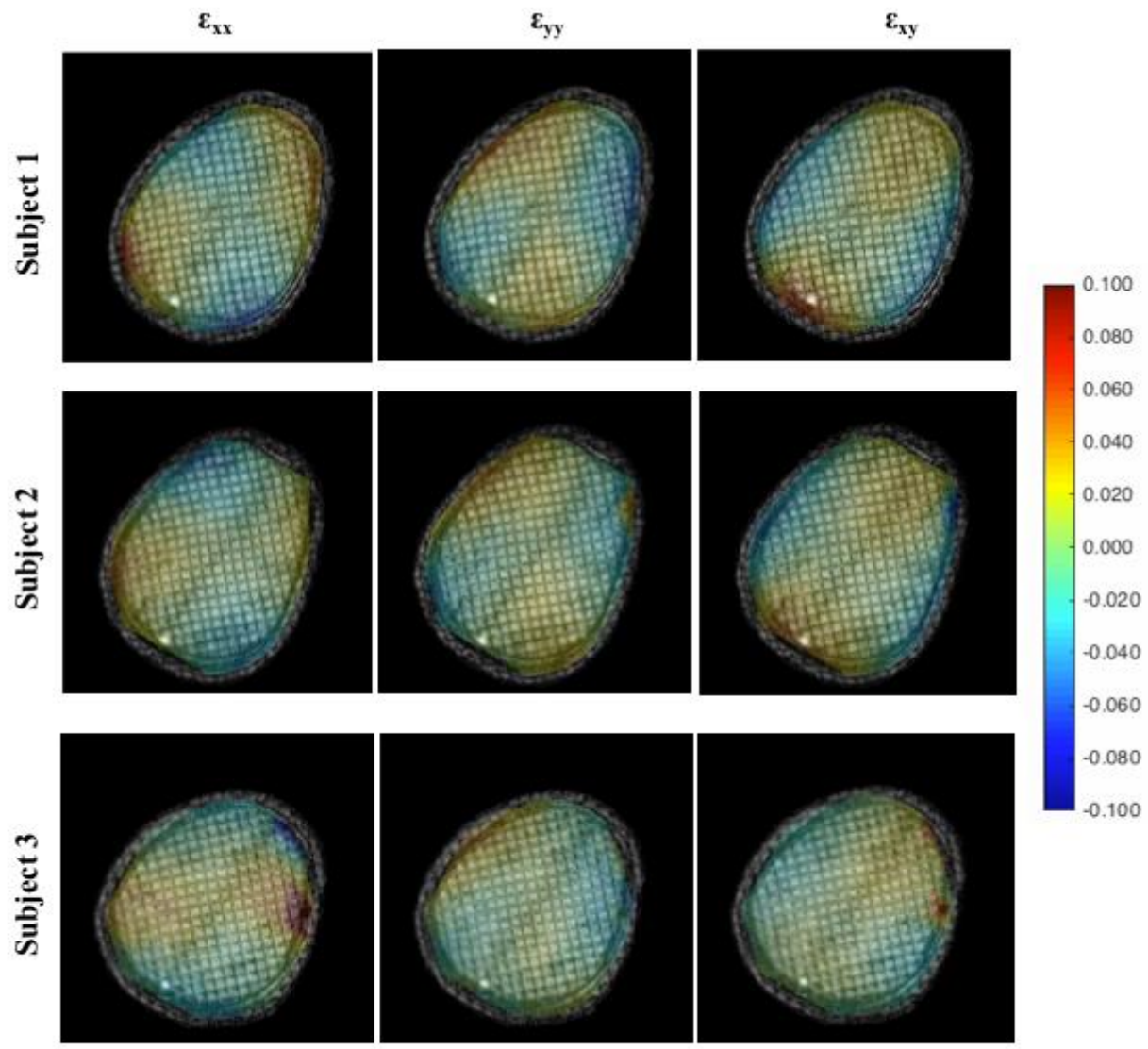

Figure 3 | Components of the Lagrangian strain tensor using DDE and SIMPLE algorithms. Tagged human brain MR-Images at moment of peak positive rotation.

We used the same data to generate principal strains for all three subjects at peak positive rotation, and observed slight variations in strain distributions at the brain-skull interface across the three subjects. Strain fields for subject 1 revealed elevated levels of first principal strain at the brain-skull interface of the left hemisphere (Fig. 4-a), and elevated levels of second principal strain at the interface of the right hemisphere (Fig. 4-b). Subject 2 revealed similar levels of first principal strain at the interface of the left hemisphere, but also presented elevated first principal strains in the right hemisphere. In subject 3, we observed a high concentration of first principal strain at the proximal end of the right hemisphere, in the same location where we observed high levels of normal and shear strains in Cartesian coordinates.

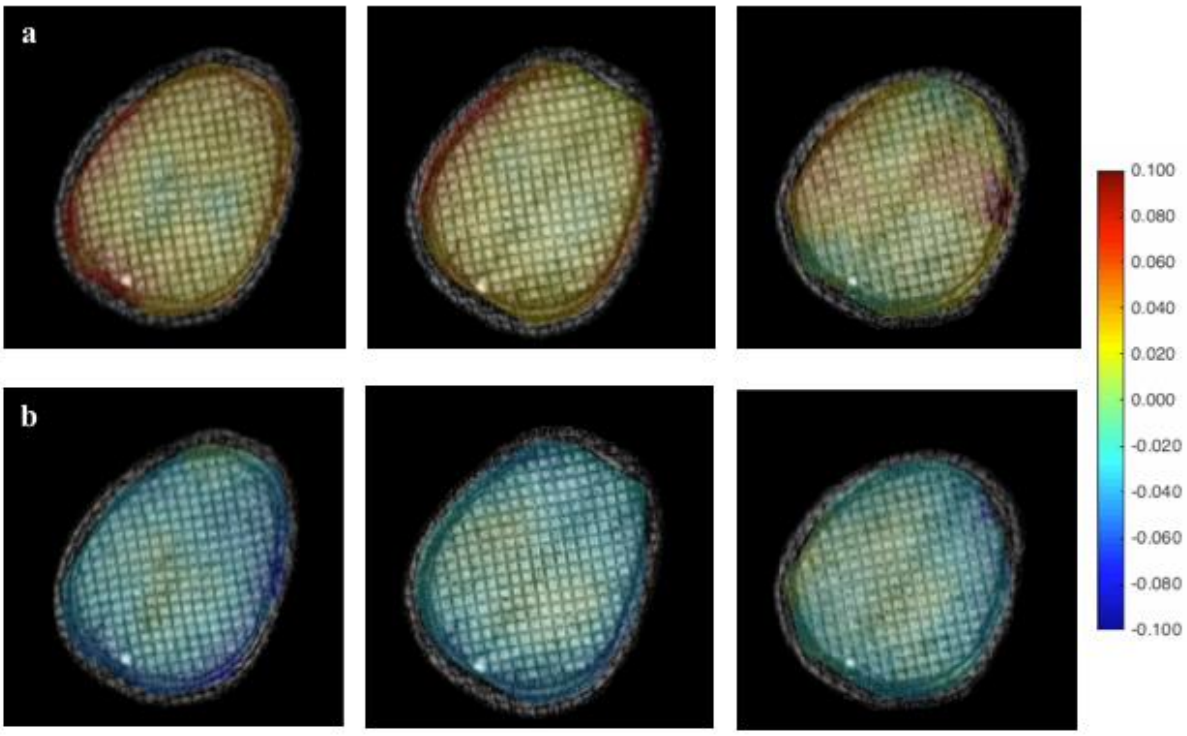

Figure 4 | Analysis of principal strains in human brain during deformation inside the skull. (a) First principal strains taken at peak rotation. **(b)** Second principal strains taken at peak rotation. From left to right: Subject 1, Subject 2, Subject 3.

3.3 Brain rotation at the brain-skull interface reveals elevated strains in the sub-arachnoid space

We quantified the strains found at the brain-skull interface, and observed significantly elevated strains along the periphery of the brain, where connective tissue is located. Strains located at the interface ranged from 1.25 – 1.5 times greater than the average strains along the brain parenchyma (Fig. 6). 2 cm above the corpus callosum, the connective tissue on the periphery of the brain is composed primarily of sub-arachnoid space, a level of support between the dura mater and arachnoid mater characterized by CSF and blood vessels. Our results revealed significantly elevated strains (characterized by a 99% confidence interval *p*-test) along this area, with varying concentrations of large strains at different locations along the circumference of each subject's sub-arachnoid space.

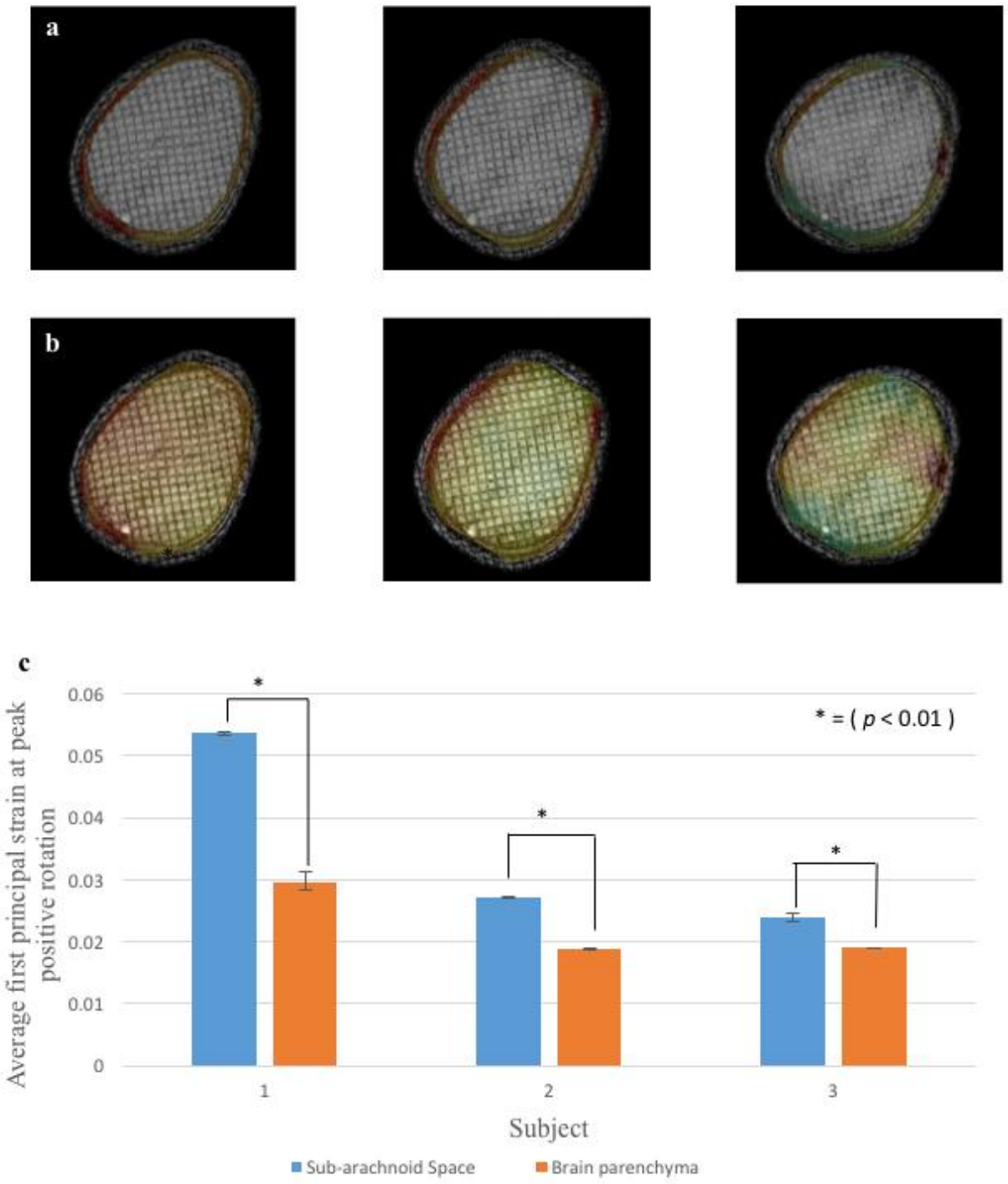

Figure 5 | Sub-arachnoid space insulates brain from rotation. (a) DDE lines tracking deformation in the sub-arachnoid space between the brain parenchyma and skull (from left to right: subject 1, subject 2, subject 3). **(b)** DDE lines tracking deformation of the brain parenchyma (from left to right: subject 1, subject 2, subject 3). **(c)** Quantitative comparison of principal strains in the sub-arachnoid space to the strains found across the brain parenchyma.

4. Discussion

4.1 Differences in strain patterns between the brain and a gel phantom provide insight into the brain's mechanical support system within the skull

In the human subjects, we observed high concentrations of strains in the sub-arachnoid space, an area that is absent from the gel phantom studies. We attribute this rise in strain magnitude to the relative compliance associated with this region, due mainly to the presence of CSF and associated slippage between the arachnoid mater and dura mater. In Subject 1, we observed an even distribution of principal strains, with high first principal strains around the left hemisphere, and high second principal strains around the right hemisphere. These results are expected from a clockwise rotation of the brain, which we hypothesize created high levels of tension in the left hemisphere and high levels of compression in the right hemisphere. Additionally, the *falx cerebri*, which is connected to the dura mater and arachnoid mater, acts as additional support to the brain, and serves to restrict motion. As a result, we hypothesize that the observed high levels of compression near the *falx* in the right hemisphere are a result of the *falx* inhibiting brain rotation.

4.2 Skull shape affects transmission of strains throughout the brain, particularly within the sub-arachnoid space

In subject 1, we observed a smooth and equal distribution of principal strains, attributed to general anatomy of the brain and connective tissue. In subjects 2 and 3, we observed a more complex distribution of strains which did not conform with the mechanical behavior of subject 1. We attribute this variation in strain patterns to the associated variation in skull shape between subjects. We observed that a narrower curvature at the proximal end of the skull results in smoother brain movement, and wider curvature of the proximal end of the skull hinders this motion, creating elevated strains in unexpected areas. Subject 2 revealed elevated first principal strains in the periphery of both the left and right hemispheres, which we attribute to the wider skull shape, prompting tension to arise between the right hemisphere and the skull during rotation. Subject 3 supports this hypothesis as well, presenting with a significantly wider skull shape and a lack of symmetry in the strain distributions throughout the sub-arachnoid space.

Additionally, subject 3 has a skull with a temporal fossa curvature that is significantly different from subjects 1 and 2. A small region of convexity in the right hemisphere is evident, which created abnormal movement of the brain during controlled rotation. The highest concentration of principal strain was found at the porton of the sub-arachnoid space directly inside of this convex skull curvature. It was also in this location that we observed a high concentration of normal (ε_{xx}) and shear (ε_{xy}) strains. We hypothesize that this convex portion of the skull arrested motion of the brain prematurely, and caused the lack of compression near the *falx cerebri*.

4.3 Skull shape affects sensitivity to acceleration amongst individuals

The results from this study not only suggest that the distribution of strains are affected by skull shape, but that skull shape in general can directly affect an individual's sensitivity to brain deformation. The strain fields generated from subject 3 reveal that even a small convexial curvature can induce substantial strain magnitudes, and significantly alter the mechanical response inside the skull. These findings constitute a possible mechanism for acceleration sensitivity among individuals, and reveal that skull shape has the potential to affect an individual's susceptibility to brain injury.

5. Conclusion

In this study, we presented a novel strain measurement algorithm that is able to circumvent the limitations of Fourier-based techniques and accurately analyze strains at the periphery of irregularly shaped objects. We applied this technique to tagged MR-images of human brains and successfully obtained strain fields at the brain-skull interface, gaining insight into the mechanical behavior of the brain inside the skull for the first time. We found substantial stress relief at the brain-skull interface, attributed to the sliding that occurs between the arachnoid mater and dura mater, as well as the CSF present in the sub-arachnoid space. We also observed arrested brain motion near the *falx cerebri*, which resulted in high magnitudes of strains at the distal end of the brain. From here, we were able to identify key factors that cause variations in stress and strain distributions from patient to patient. Specifically, we found that skull shape plays a key role in determining the symmetry of strains across the brain parenchyma, as well as the even distribution of principal strains in the sub-arachnoid space. We observed that convex curvature of the skull served to arrest brain motion, resulting in high magnitudes of strain. These results suggest that certain factors (i.e. skull shape) may make an individual experience significantly higher strain when exposed to rapid head acceleration, and as a result make them more susceptible to TBI.

Works Cited

1. Pearson, W.; Sugerman, D.; Mcguire, L.; Coronado, V. Emergency Department Visits for Traumatic Brain Injury in Older Adults in the United States: 2006-08. *Western Journal of Emergency Medicine*2012, *13*(3), 289–293 DOI: 10.5811/westjem.2012.3.11559.

2. Finkelstein, E. A.; Corso, P. S.; Miller, T. R. The Burden of Injuries. *The Incidence and Economic Burden of Injuries in the United States*2006, 160–174 DOI: 10.1093/acprof:oso/9780195179484.003.0005.

3. Coronado VG, McGuire LC, Faul M, Sugerman D, Pearson W. "The epidemiology and prevention of TBI." In press.

4. T.A. Gennarelli, L.E. Thibault, R. Tipperman, G. Tomei, R. Sergot, M. Brown, W.L. Maxwell, D.I. Graham, J.H. Adams, A. Irvine,*et al.* Axonal injury in the optic nerve: a model simulating diffuse axonal injury in the brain *Journal of Neurosurgery*, 71 (2) (1989), pp. 244–253.

5. A.C. Bain, D.F. Meaney. Tissue-level thresholds for axonal damage in an experimental model of central nervous system white matter injury. *Journal of Biomechanical Engineering*, 122 (2000), pp. 615–622.

6. Knowles, B. M.; Yu, H.; Dennison, C. R. Accuracy of a Wearable Sensor for Measures of Head Kinematics and Calculation of Brain Tissue Strain. *Journal of Applied Biomechanics* **2016**, 1–34 DOI: 10.1123/jab.2016-0026.

7. Li, D.; Ma, C.; Shen, M.; Li, P.; Zhang, J. Brain Injury Differences in Frontal Impact Crash Using Different Simulation Strategies. *Computational and Mathematical Methods in Medicine* **2015**, *2015*, 1–8 DOI: 10.1155/2015/348947.

8. Kimpara, H.; Iwamoto, M. Mild Traumatic Brain Injury Predictors Based on Angular Accelerations During Impacts. *Annals of Biomedical Engineering* **2011**, *40* (1), 114–126 DOI: 10.1007/s10439-011-0414-2.

9. Bayly, P. V.; Clayton, E. H.; Genin, G. M. Quantitative Imaging Methods for the Development and Validation of Brain Biomechanics Models. *Annual Review of Biomedical Engineering* **2012**, *14* (1), 369–396 DOI: 10.1146/annurev-bioeng-071811-150032.

10. Massouros, P. G.; Bayly, P. V.; Genin, G. M. Strain localization in an oscillating Maxwell viscoelastic cylinder. *International Journal of Solids and Structures* **2014**, *51* (2), 305–313 DOI: 10.1016/j.ijsolstr.2013.09.022.

11. Bayly, P.; Massouros, P.; Christoforou, E.; Sabet, A.; Genin, G. Magnetic resonance measurement of transient shear wave propagation in a viscoelastic gel cylinder. *Journal of the Mechanics and Physics of Solids* **2008**, *56* (5), 2036–2049 DOI: 10.1016/j.jmps.2007.10.012.

12. Sabet, A. A.; Christoforou, E.; Zatlin, B.; Genin, G. M.; Bayly, P. V. Deformation of the human brain induced by mild angular head acceleration. *Journal of Biomechanics* **2008**, *41* (2), 307–315 DOI: 10.1016/j.jbiomech.2007.09.016.

13. Knutsen, A. K.; Magrath, E.; Mcentee, J. E.; Xing, F.; Prince, J. L.; Bayly, P. V.; Butman, J. A.; Pham, D. L. Improved measurement of brain deformation during mild head acceleration using a novel tagged MRI sequence. *Journal of Biomechanics* **2014**, *47* (14), 3475–3481 DOI: 10.1016/j.jbiomech.2014.09.010.

14. Downes, J. R.; Faux, D. A. The Fourier-series method for calculating strain distributions in two dimensions. *Journal of Physics: Condensed Matter* **1997**, *9* (22), 4509–4520 DOI: 10.1088/0953-8984/9/22/004.

15. Bayly, P. V.; Black, E. E.; Pedersen, R. C.; Leister, E. P.; Genin, G. M. In vivo imaging of rapid deformation and strain in an animal model of traumatic brain injury. *Journal of Biomechanics* **2006**, *39* (6), 1086–1095 DOI: 10.1016/j.jbiomech.2005.02.014.

16. Eldeeb, S. M.; Fahmy, A. S. Accurate harmonic phase tracking of tagged MRI using locally-uniform myocardium displacement constraint. *Medical Engineering & Physics* **2016**, *38* (11), 1305–1313 DOI: 10.1016/j.medengphy.2016.08.002.

17. Boyle, J. J.; Kume, M.; Wyczalkowski, M. A.; Taber, L. A.; Pless, R. B.; Xia, Y.; Genin, G. M.; Thomopoulos, S. Simple and accurate methods for quantifying deformation, disruption, and development in biological tissues. Journal of The Royal Society Interface 2014, 11 (100), 20140685–20140685 DOI: 10.1098/rsif.2014.0685.

18. Axel L, Dougherty L. MR imaging of motion with spatial modulation of magnetization. Radiology.1989;171(3):841–845.